

Primary particle acceleration above 100 TeV in the shell-type supernova remnant RX J1713.7–3946 with deep HESS observations

F. Aharonian¹, A. G. Akhperjanian², A. R. Bazer-Bachi³, M. Beilicke⁴, W. Benbow¹, D. Berge^{1,*}, K. Bernlöhr^{1,5}, C. Boisson⁶, O. Bolz¹, V. Borrel³, I. Braun¹, E. Brion⁷, A. M. Brown⁸, R. Bühler¹, I. Büsching⁹, S. Carrigan¹, P. M. Chadwick⁸, L.-M. Chouet¹⁰, G. Coignet¹¹, R. Cornils⁴, L. Costamante^{1,23}, B. Degrange¹⁰, H. J. Dickinson⁸, A. Djannati-Atai¹², L. O’C. Drury¹³, G. Dubus¹⁰, K. Egberts¹, D. Emmanoulopoulos¹⁴, P. Espigat¹², F. Feinstein¹⁵, E. Ferrero¹⁴, A. Fiasson¹⁵, G. Fontaine¹⁰, Seb. Funk⁵, S. Funk¹, M. Füßling⁵, Y. A. Gallant¹⁵, B. Giebels¹⁰, J. F. Glicenstein⁷, B. Glück¹⁶, P. Goret⁷, C. Hadjichristidis⁸, D. Hauser¹, M. Hauser¹⁴, G. Heinzlmann⁴, G. Henri¹⁷, G. Hermann¹, J. A. Hinton^{1,14,**}, A. Hoffmann¹⁸, W. Hofmann¹, M. Holleran⁹, S. Hoppe¹, D. Horns¹⁸, A. Jacholkowska¹⁵, O. C. de Jager⁹, E. Kendziorra¹⁸, M. Kerschhaggl⁵, B. Khélifi^{10,1}, Nu. Komin¹⁵, A. Konopelko^{5,***}, K. Kosack¹, G. Lamanna¹¹, I. J. Latham⁸, R. Le Gallou⁸, A. Lemièrre¹², M. Lemoine-Goumard¹⁰, T. Lohse⁵, J. M. Martin⁶, O. Martineau-Huynh¹⁹, A. Marcowith³, C. Masterson^{1,23}, G. Maurin¹², T. J. L. McComb⁸, E. Moulin¹⁵, M. de Naurois¹⁹, D. Nedbal²⁰, S. J. Nolan⁸, A. Noutsos⁸, J.-P. Olive³, K. J. Orford⁸, J. L. Osborne⁸, M. Panter¹, G. Pelletier¹⁷, S. Pita¹², G. Pühlhofer¹⁴, M. Punch¹², S. Ranchon¹¹, B. C. Raubenheimer⁹, M. Raue⁴, S. M. Rayner⁸, A. Reimer²¹, O. Reimer[†], J. Ripken⁴, L. Rob²⁰, L. Rolland⁷, S. Rosier-Lees¹¹, G. Rowell^{1,‡}, V. Sahakian², A. Santangelo¹⁸, L. Saugé¹⁷, S. Schlenker⁵, R. Schlickeiser²¹, R. Schröder²¹, U. Schwanke⁵, S. Schwarzburg¹⁸, S. Schwemmer¹⁴, A. Shalchi²¹, H. Sol⁶, D. Spangler⁸, F. Spanier²¹, R. Steenkamp²², C. Stegmann¹⁶, G. Superina¹⁰, P. H. Tam¹⁴, J.-P. Tavernet¹⁹, R. Terrier¹², M. Tluczykont^{10,23}, C. van Eldik¹, G. Vasileiadis¹⁵, C. Venter⁹, J. P. Vialle¹¹, P. Vincent¹⁹, H. J. Völk¹, S. J. Wagner¹⁴, and M. Ward⁸

(Affiliations can be found after the references)

Received 11 September 2006 / Accepted 22 November 2006

ABSTRACT

Aims. We present deep HESS observations of the supernova remnant (SNR) RX J1713.7–3946. Combining data of three years – from 2003 to 2005 – we obtain significantly increased statistics and energy coverage as compared to earlier 2003 and 2004 results.

Methods. The data are analysed separately for the different years.

Results. Very good agreement of the gamma-ray morphology and the differential spectra is found when comparing the three years. The combined gamma-ray image of the 2004 and 2005 data reveals the morphology of RX J1713.7–3946 with unprecedented precision. An angular resolution of 0.06° is achieved, revealing the detailed structure of the remnant. The combined spectrum of all three years extends over three orders of magnitude, with significant gamma-ray emission approaching 100 TeV. The cumulative significance above 30 TeV is 4.8σ, while for energies between 113 and 294 TeV an upper limit on the gamma-ray flux of 1.6 × 10⁻¹⁶ cm⁻² s⁻¹ is obtained.

Conclusions. The energy coverage of the HESS data is presumably at the limit of present generation Cherenkov telescopes. The measurement of significant gamma-ray emission beyond 30 TeV formally implies the existence of primary particles of at least that energy. However, for realistic scenarios of very-high-energy gamma-ray production, the Inverse Compton scattering of very-high-energy electrons and π⁰ decay following inelastic proton-proton interactions, the measured gamma-ray energies imply that efficient acceleration of primary particles to energies exceeding 100 TeV is taking place in the shell of the SNR RX J1713.7–3946.

Key words. acceleration of particles – ISM: cosmic rays – gamma rays: observations – ISM: supernova remnants

1. Introduction

The energy spectrum of cosmic rays measured at Earth exhibits a power-law dependence over a broad energy range. Starting at a few GeV (1 GeV = 10⁹ eV) it continues to energies of at least 10²⁰ eV. The power-law index of the spectrum changes at two characteristics energies: in the region around 3 × 10¹⁵ eV – the *knee* region – the spectrum steepens, and at energies beyond 10¹⁸ eV it hardens again. This latter feature is known as the *ankle*. Up to the knee, cosmic rays are believed to be of Galactic origin, accelerated in shell-type supernova remnants (SNRs) –

* Now at CERN, Geneva, Switzerland.

** Now at School of Physics & Astronomy, University of Leeds, Leeds LS2 9JT, UK.

*** Now at Purdue University, Department of Physics, 525 Northwestern Avenue, West Lafayette, IN 47907-2036, USA.

† Now at Stanford University, HEPL & KIPAC, Stanford, CA 94305-4085, USA.

‡ Now at School of Chemistry & Physics, University of Adelaide, Adelaide 5005, Australia.

expanding shock waves initiated by supernova explosions (for a recent review see Hillas 2005). However, the experimental confirmation of an SNR origin of Galactic cosmic rays is difficult due to the propagation effects of charged particles in the interstellar medium. The most promising way of proving the existence of high-energy particles in SNR shells is the detection of very-high-energy (VHE) gamma rays ($E > 100$ GeV), produced in interactions of cosmic rays close to their acceleration site (Drury et al. 1994).

Recently HESS – a VHE gamma-ray instrument consisting of four Imaging Atmospheric Cherenkov Telescopes – has detected two shell-type SNRs, RX J1713.7–3946 (Aharonian et al. 2004b, 2006b) and RX J0852.0–4622 (Aharonian et al. 2005a). The two objects show an extended morphology and exhibit a shell structure, as expected from the notion of particle acceleration in the expanding shock fronts. Both objects reveal gamma-ray spectra that can be described by a hard power law (with photon index $\Gamma \sim 2.0$) over a broad energy range. For RX J1713.7–3946 significant deviations from a pure power law at larger energies are measured (Aharonian et al. 2006b). While it is difficult to attribute the measured VHE gamma rays unambiguously to nucleonic cosmic rays (rather than to cosmic electrons, which would certainly also be accelerated in the shock front), the measured spectral shapes favour indeed in both cases – for RX J1713.7–3946 and RX J0852.0–4622 – a nucleonic cosmic-ray origin of the gamma rays (Aharonian et al. 2006a,b). In the case of RX J1713.7–3946 in addition a narrow shock filament seen in X-rays (Hiraga et al. 2005) indicates strong amplification of the magnetic field at least in one region of the rim (Berezhko & Völk 2006). If such an amplified magnetic field exists throughout the main volume of the SNR – the region for which VHE gamma-ray data is presented here – and if consequently high magnetic field values are found not only in one shock filament, but on a large part of the shock surface, a leptonic origin of the VHE gamma rays becomes increasingly unlikely just based on the absolute level of X-ray and gamma-ray flux of RX J1713.7–3946 (Aharonian et al. 2006b).

Apart from the first unambiguous proof of multi-TeV particle acceleration in SNRs (Aharonian et al. 2006a,b), the question of the highest observed energies remains an important one. Only the detection of gamma rays with energies of 100 TeV and beyond provides experimental proof of acceleration of primary particles, protons or electrons, to even higher energies of 1 PeV and beyond. The spectrum of the whole SNR RX J1713.7–3946 reported in Aharonian et al. (2006b) comprises data of the 2004 observation campaign of HESS. It extends to energies of 40 TeV. Here we present a combined analysis of HESS data of RX J1713.7–3946 recorded in three years, in 2003 during the construction and commissioning phase of the system, and in 2004 and 2005 with the full HESS array. A comparison of the three data sets demonstrates the expected steady emission of the source as well as the stability of the system during the first three years of running. Special emphasis is then devoted to the high-energy end of the combined spectrum.

2. HESS observations

The High Energy Stereoscopic System (HESS) consists of four identical Cherenkov telescopes that are operated in the Khomas Highland of Namibia (Hofmann 2005). The telescopes (Bernlöhr et al. 2003; Cornils et al. 2003) are 13 m in diameter, each with a mirror area of 107 m². During normal operation the system is run in a coincidence mode which requires a trigger from at least two out of the four telescopes (Funk et al. 2004). The

cameras consist of 960 photomultiplier pixels and cover a 5° field of view (Vincent et al. 2003). The resulting $FWHM \approx 4^\circ$ of the system field-of-view response makes HESS the currently best suited experiment in the field for the study of extended VHE gamma-ray sources such as young Galactic SNRs. At zenith, the energy threshold is about 100 GeV and for point sources an energy resolution of 15% is achieved. The angular resolution for individual gamma rays is better than 0.1° and the point source sensitivity reaches 1% of the flux of the Crab nebula for long exposures (~25 h).

The HESS observation campaign of RX J1713.7–3946 started in 2003. The data were recorded between May and August 2003 during two phases of the commissioning of the telescope system. During the first phase, two telescopes were operated independently with stereoscopic event selection done offline using GPS time stamps to identify coincident events. During the second phase, also using two telescopes, coincident events were selected in hardware using the array level trigger (Funk et al. 2004). The observations were performed in Declination wobble mode around the northwest shell of the SNR, the alternating wobble offset in Declination was 0.5°. The zenith angle of observations varied from 15° to 30° with a mean of 24°. The analysis of this first data set revealed extended gamma-ray emission resembling a shell structure, very similar to the X-ray image. It was actually the first ever resolved image of an astronomical source obtained with VHE gamma rays (Aharonian et al. 2004b). The spectrum was well described by a hard power law with energies from 1 to 10 TeV.

In 2004, observations were conducted with the full telescope array. From April to May, most of the data were recorded in wobble mode, this time around the SNR centre with an offset of 0.7° in Right Ascension and Declination aiming at more uniform coverage of the whole SNR and, important for analysis purposes, fully encompassing the SNR with the four observation positions. The zenith angle of observations ranged from 16° to 56° with a mean of 26°. The HESS data enabled analysis of the gamma-ray morphology and the spectrum of the remnant with unprecedented precision (Aharonian et al. 2006b). A very good correlation was found between the X-ray and the gamma-ray image. The differential spectrum was measured from 200 GeV up to 40 TeV. A deviation from a pure power law was found at high energies. A spatially resolved spectral study revealed no significant changes of spectral shape across the SNR despite flux variations by more than a factor of two.

The 2005 observation campaign was aiming at extending the energy coverage of the spectrum to as high energies as possible. Therefore the observations, carried out from beginning of September to November, were preferentially pursued at large zenith angles, up to values of 70°, to make use of the drastically increased effective collection area of the experiment at high energies. The mean zenith angle of observations was 51°. As in 2004, RX J1713.7–3946 was observed in wobble mode with an offset of 0.7° in Declination and Right Ascension. Analysis of these data are for the first time presented in the following. A summary of the observations conducted during three years with HESS is given in Table 1.

3. Data analysis

The RX J1713.7–3946 data presented here are calibrated according to the standard HESS calibration methods (Aharonian et al. 2004a). For the background suppression, cuts on scaled image parameters are applied (Aharonian et al. 2005b). The shower reconstruction is based on image parameters (Hillas

Table 1. Summary of HESS observations of RX J1713.7–3946 conducted during three years. For each year, the targeted position is given together with the wobble offsets in Right Ascension (α_{J2000}) and Declination (δ_{J2000}). Adding the wobble offsets to the target coordinates, the actual pointing position is obtained. For each pointing position, the dead-time corrected observation time (*Live time*) is given in hours. Data recorded under bad weather conditions are excluded. The columns *Data set I-III* summarise observation times of data sub-sets used throughout the paper. *Data set I* is used for Fig. 2; to obtain optimum angular resolution, the 2003 data are disregarded and a zenith-angle cut at 60° is applied (the latter is only relevant for the 2005 data). *Data set II* is used for spectral comparisons of the different years (cf. Fig. 3). Observations with wobble offsets of 0° in 2004 and 2005 are disregarded for this purpose. *Data set III* comprises all data, and is used for the generation of the combined spectrum (cf. Fig. 4).

Year	Target position		Wobble offsets		Live time (h)	Data set I	Data set II	Data set III
	α_{J2000}	δ_{J2000}	$\Delta\alpha_{J2000}$	$\Delta\delta_{J2000}$		<i>best-resolution data</i> (h)	<i>spectral comparisons</i> (h)	<i>all data</i> (h)
2003	17h12m00s	$-39^\circ 39' 00''$	0°	$+0.5^\circ$	9.1	0	18.1	18.1
			0°	-0.5°	9.0			
			0°	$+0.7^\circ$	7.3			
2004	17h13m33s	$-39^\circ 45' 44''$	0°	-0.7°	8.1	33.1	30.6	33.1
			$+0.7^\circ$	0°	6.9			
			-0.7°	0°	8.3			
			0°	0°	2.5			
			0°	$+0.7^\circ$	9.0			
2005	17h13m33s	$-39^\circ 45' 44''$	0°	-0.7°	9.5	29.7	36.8	40.1
			$+0.7^\circ$	0°	8.7			
			-0.7°	0°	9.4			
			0°	0°	3.5 ¹			

¹ These observations had wobble offsets of 0.5° in Right Ascension and Declination, less than the radius of the SNR, and are summarised in one row.

parameters) and corresponds, unless otherwise stated, to *algorithm 1* of Hofmann et al. (1999): the intersection point of the image axes in a common camera coordinate system yields the shower impact position on ground and the direction of the primary. A cut on the minimum size of camera images is applied to assure that only well defined images are included in the analysis. For the 2003 two-telescope data, the cut is applied at a rather large value of 300 photo-electrons. In the commissioning phase of the experiment, this served to dramatically reduce the number of background events, but it also homogenises the whole data set, which was recorded with two different hardware configurations, thereby reducing systematic uncertainties. Moreover, the angular resolution improves when including only well defined images in the analysis. The 2004 and 2005 data are analysed as discussed in Aharonian et al. (2006b). For spectral analysis, a loose cut on the minimum image size at 80 photo-electrons is applied. For studies of the gamma-ray morphology, the cut is increased to 200 photo-electrons yielding superior angular resolution of the order of 0.08° and better background suppression.

For the subtraction of the irreducible cosmic-ray background, separate approaches are taken for the generation of gamma-ray spectra and images. The preferred background-estimation method for spectral analysis is the *reflected-region* model (Hinton et al. 2005). The background estimate is derived from a region of the same size and shape as the source region, reflected at the system pointing direction. To assure non-overlapping source and background-control regions, this approach can only be applied if the observation positions have been chosen outside the nominal gamma-ray source region. As can be seen from Table 1, this is not true for the whole 2003 data and parts of the 2004 and 2005 observations. For these data, an *ON/OFF*-background model is applied instead. From the complete set of HESS observations without gamma-ray signal, *OFF* runs for background estimation are selected with zenith-angle distributions matching that of the *ON* runs as close as possible.

For image generation, the *field-of-view*-background model is applied (Hinton et al. 2005). It models the background by means of a system acceptance model determined from the full

set of HESS *OFF* runs. The normalisation is calculated using the whole field of view excluding regions of known gamma-ray emission. Note that the background-subtracted gamma-ray images shown throughout this paper are smoothed with a Gaussian to reduce statistical fluctuations. The resulting images are in units of gamma-ray excess counts per Gaussian sigma. They are corrected for the falloff of the system acceptance towards the edges of the field of view which results from a smaller detection efficiency far from the pointing centre.

When determining spectra of the whole SNR, a circular region of 0.65° radius is used here, centred at $\alpha_{J2000} = 17\text{h}13\text{m}33.6\text{s}$, $\delta_{J2000} = -39^\circ 45' 36''$.

4. Gamma-ray morphology

The gamma-ray morphology as obtained from the HESS data of three years is seen in the upper panel of Fig. 1. For the 2003 data, a special set of analysis cuts was applied adopted to the two-telescope data (cf. Sect. 3). For the 2005 image, only observations at zenith angles smaller than 60° are taken into account (reducing the available observation time by ~ 10 h, cf. Table 1). For larger zenith-angle observations, the geometrical reconstruction worsens, deteriorating the angular resolution of the resulting image.

The images of Fig. 1 are readily comparable. They are corrected for system acceptance, which is different for the different data because of the zenith-angle dependence of the acceptance and the intermediate system configuration of 2003. Very similar angular resolutions are achieved for all years, see Table 2, where relevant parameters are listed. From the visual impression the three images shown in the figure are very similar. Within statistics, good agreement is achieved, as can be seen from the one-dimensional distributions shown in the lower panel of Fig. 1, which have the advantage that statistical errors on the measurement can be taken into account for the comparison. Shown from left to right are a slice along a thick box (shown in the upper panel of Fig. 1), an azimuthal profile of the shell region, and a radial profile. All the distributions are generated from the

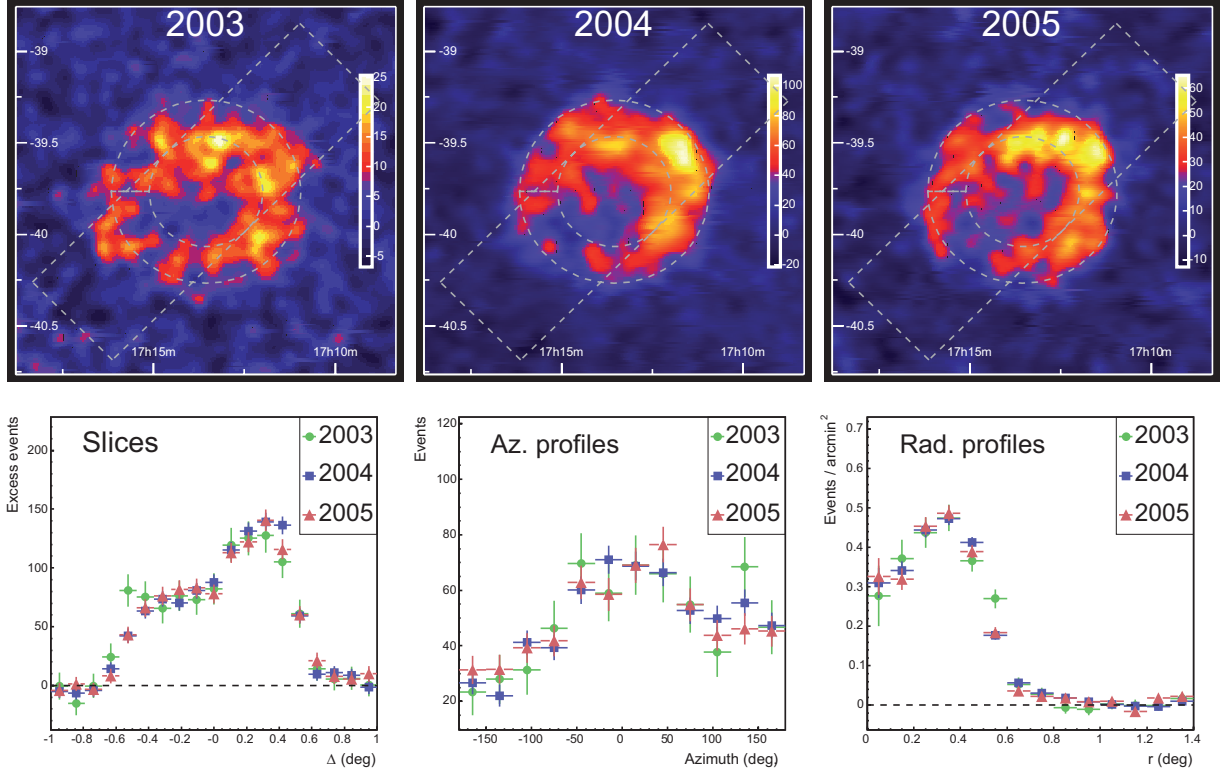


Fig. 1. *Upper panel:* HESS gamma-ray excess images from the region around RX J1713.7–3946 are shown for each year separately for comparison. From left to right, images are generated from data of 2003, 2004 and 2005. The images are corrected for the decline of the system acceptance with increasing distance to the SNR centre. All three images are smoothed with a Gaussian of $2'$, the linear colour scale is in units of excess counts per smoothing radius. The dashed box (dimensions $2^\circ \times 0.6^\circ$) and ring ($r_1 = 0.3^\circ$, $r_2 = 0.5^\circ$) are used for obtaining the one-dimensional distributions shown in the lower panel. *Lower panel:* one-dimensional distributions for the data of three years, all generated from the raw, non-smoothed and acceptance-corrected gamma-ray excess images. Histograms of 2004 and 2005 are scaled to the area of the 2003 histogram to account for differences in the event statistics. *Left:* slices taken within a rotated box running through the SNR region. Plotted are events versus angular distance to the centre, projected onto the axis running through the SNR centre, rotated by 45° anti-clockwise with respect to the RA axis. *Middle:* azimuth profiles integrated in a thick ring covering the shell of RX J1713.7–3946. The azimuthal angle of the events is calculated with respect to the SNR centre ($\alpha_{J2000} = 17h13m33.6s$, $\delta_{J2000} = -39^\circ 45' 36''$). 0° corresponds to the west part of the shell, 90° is north or upward, -90° is south or downward. *Right:* radial profiles around the centre of the SNR. Plotted are excess events per unit solid angle as a function of the distance r to the SNR centre.

Table 2. Summarised are the event statistics of the whole SNR and corresponding angular resolutions for the years 2003, 2004, and 2005. The 2004 and 2005 data sets correspond to *Data set I* of Table 1. The average zenith angle ($\langle\phi_z\rangle$) is determined from all events reconstructed in the SNR region. For the angular resolution (R_{68}), the 68% containment radius of the simulated gamma-ray point-spread function, matched to the particular data set, is used as figure of merit. The other columns give the number of signal events from the SNR region (ON), the number of background events (OFF), the normalisation factor between ON and OFF counts (α), and the corresponding significance and live observation time. α is in general defined as the ratio of the effective exposure integrated in time and angular space of the ON and OFF region. Note that the analysis of the 2003 data is adopted to match the system configuration of this year. The nominal analysis is applied for the 2004 and 2005 data. For 2005, only data recorded at zenith angles less than 60° are included (therefore the mean zenith angle decreases). The event statistics are determined with the *ON/OFF* approach for 2003 and the *reflected-region* method for 2004 and 2005. In the latter two years, also *ON* runs with wobble offsets $<0.7^\circ$ (cf. Table 1) are included and hence $\alpha > 1$.

Year	$\langle\phi_z\rangle$	R_{68}	ON	OFF	α	Significance (σ)	Live time (h)
2003	24°	0.083°	3194	1764	1.00	21	18.1
2004	27°	0.075°	18728	11039	1.05	41	33.1
2005	44°	0.082°	10277	5124	1.15	33	29.7

non-smoothed, acceptance-corrected excess images, very finely binned such that binning effects are negligible. Clearly, there is no sign of disagreement or variability, the HESS data of three years are well compatible with each other.

The combined HESS image is shown in Fig. 2. Data of 2004 and 2005 are used for this smoothed, acceptance-corrected gamma-ray excess image (*Data set I* in Table 1). In order to obtain optimum angular resolution, a special analysis is applied here. In addition to the image-size cut of 200 photo-electrons,

the cut on the minimum event multiplicity is raised to three telescopes (disregarding the 2003 data for this purpose completely). Moreover, an advanced reconstruction method is chosen. It takes Monte-Carlo error estimates on image parameters into account and is based on *algorithm 3* of Hofmann et al. (1999) (see Berge (2006) for studies of this analysis technique). The image corresponds to 62.7 h of dead-time corrected observation time. With the *reflected-region* method, 12961 ON events from the region associated with the SNR are accumulated, and 5710 OFF events

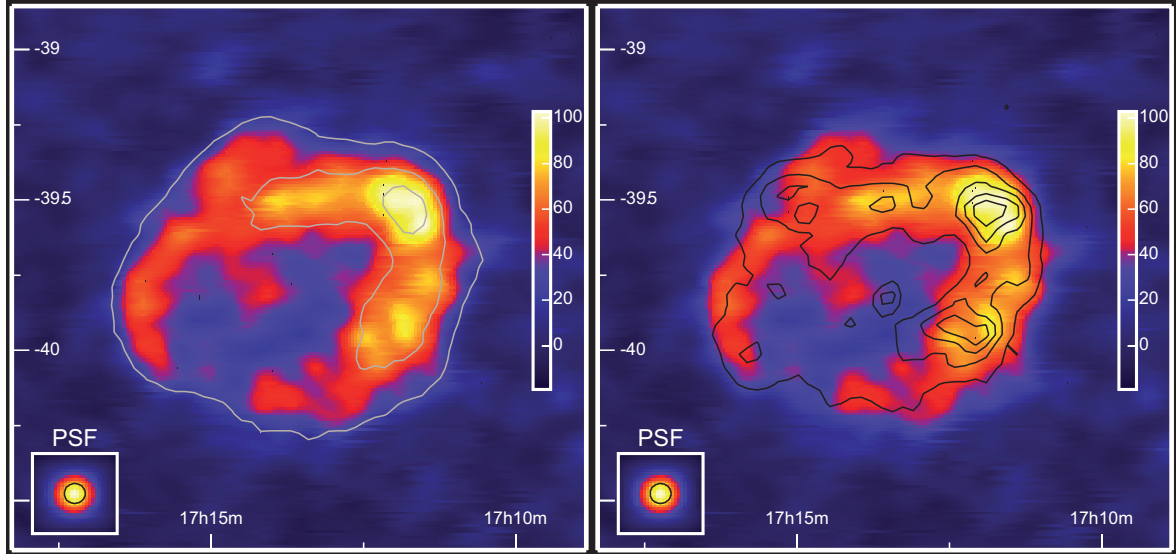


Fig. 2. Two versions of the combined HESS image from the 2004 and 2005 data. Shown is in both cases an acceptance-corrected gamma-ray excess image. The images are smoothed with a Gaussian of $2'$. A simulated point source as it would appear in this data set is shown in the lower left-hand corner of both images (labeled *PSF*). It is smoothed with the same Gaussian, the σ of $2'$ is denoted as black circle in the insets. The linear colour scale is in units of excess counts per smoothing radius. Note that for the 2005 data, only data recorded at zenith angles less than 60° are taken into account. On the *left-hand side*, the overlaid light-gray contours illustrate the significance of the different features. The levels are at 8, 18, and 24σ . The significance at each position has been calculated for a point-source scenario, integrating events in a circle of 0.1° radius around that position. On the *right-hand side*, ASCA contours are drawn as black lines (1–3 keV, from Uchiyama et al. 2002) for comparison.

(normalisation $\alpha = 1.1^1$). Hence, 6702 gamma-ray excess events are measured with a statistical significance of 48σ . An angular resolution of 0.06° ($3.6'$) is achieved. For comparison, the resolution obtained with the standard geometrical reconstruction method and a three-telescope multiplicity is 0.07° with similar event statistics. With a two-telescope multiplicity cut, the resolution with the standard reconstruction is 0.08° (with 28879 ON, 16070 OFF events, $\alpha = 1.1$, and a significance of 53σ).

The image in Fig. 2 confirms nicely the published HESS measurements (Aharonian et al. 2004b, 2006b), with 20% better angular resolution and increased statistics. The shell of RX J1713.7–3946, somewhat thick and asymmetric, is clearly visible and almost closed. As can be seen from the left-hand side of the figure, when integrating signal and background events in a circle of 0.1° radius around each trial point-source position, significant gamma-ray emission is found throughout the whole remnant. Even in the seemingly void south-eastern region it exceeds a level of 8 standard deviations. The gamma-ray brightest parts are located in the north and west of the SNR. The similarity of gamma-ray and X-ray morphology, which was already investigated in detail in Aharonian et al. (2006b) for the 2004 HESS data, is again demonstrated on the right-hand side of Fig. 2, where ASCA X-ray contours are overlaid on the HESS image.

5. Gamma-ray spectrum

The gamma-ray spectra measured with HESS in three consecutive years are compared to each other in Fig. 3. The 2003 spectrum is obtained from an *ON/OFF* analysis, with the set of special two-telescope cuts mentioned above. Note that these cuts were also applied to obtain the spectrum shown in Fig. 3 of Aharonian et al. (2004b), which stops at 10 TeV. Here, however, the 2003 spectrum extends to energies beyond 30 TeV.

¹ Note that pure *ON* runs with wobble offsets $<0.7^\circ$ are included in *Data set I* (cf. Table 1) and hence $\alpha > 1$.

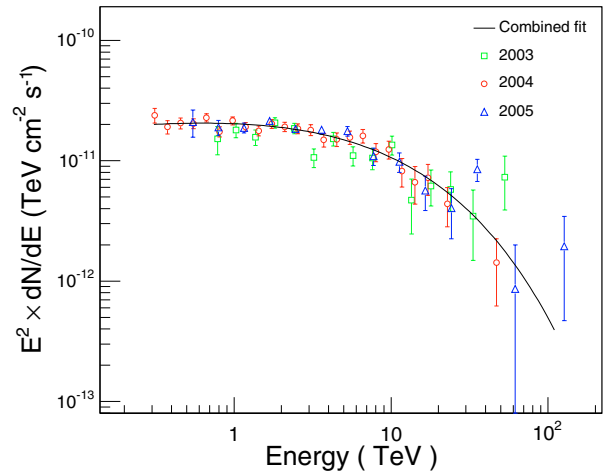


Fig. 3. Comparison of HESS spectra from the years 2003, 2004, and 2005 (*Data set II*, Table 1). The three spectra are shown in an energy-flux representation – flux points have been multiplied by E^2 . The black curve is shown for reference. It is the best fit of a power law with exponential cutoff to the combined data, where the cutoff is taken to the power of $\beta = 0.5$: $dN/dE = I_0 E^{-\Gamma} \exp(-(E/E_c)^{\beta=0.5})$. Note that flux points are corrected for the degradation of the optical efficiency of the system. The energy threshold of ~ 1 TeV in the 2003 data is due to the two-telescope operation mode and the application of a stringent cut on the minimum camera image size.

The difference between the two analyses is the energy range of simulations used to generate effective gamma-ray detection areas (needed for spectral analysis). In the old analysis, gamma rays were simulated up to 20 TeV, permitting energy reconstruction only up to ~ 10 TeV (allowing for a maximum reconstruction bias of 10%). Here, in the present analysis, simulations up to 100 TeV are available for zenith angles smaller than 60° , up to 200 TeV for angles from 60° to 63° , and up to 400 TeV for

Table 3. Comparison of event statistics from the SNR region from three years of data. The numbers result from the spectral analysis of *Data set II* (cf. Table 1), shown in Fig. 3. Given are the number of signal (*ON*) and background (*OFF*) counts, the normalisation factor α , the statistical significance of the gamma-ray excess (σ) and the observation time. For the 2003 data, the special two-telescope analysis with a cut on the minimum size of camera images at 300 photo-electrons was applied. The background estimate in this case is derived with the *ON/OFF* analysis. For 2004 and 2005, the nominal spectral analysis with a cut at 80 photo-electrons was used together with *reflected-region* background model.

Year	ON	OFF	α	Significance (σ)	Live time (h)
2003	3194	1764	1.0	20.5	18.1
2004	107494	93906	1.0	30.3	30.6
2005	71276	60175	1.0	30.6	36.8

zenith angles up to a maximum of 70° . Hence the increased energy coverage. Note that good agreement is found between the 2003 spectrum shown here and the one published previously in Aharonian et al. (2004b) in the energy range from 1 to 10 TeV.

The spectra determined from the 2004 and the 2005 data in Fig. 3 are obtained with the *reflected-region*-background model. Therefore, data where the observation position was within the SNR region are disregarded. For the purpose of comparison of the different data sets this approach seems reasonable, no attempt to analyse the remaining data with an *ON/OFF*-background approach is pursued. The corresponding event statistics for the spectra shown in the figure are listed in Table 3.

In order to compare data recorded in different years, a correction for the variation of optical efficiency of the telescope system must be applied. The efficiency degrades with time, mostly due to degradations of mirror reflectivity. As described in detail in Aharonian et al. (2006c), this worsening of the actual efficiency with respect to the simulated one causes a shift in the absolute energy scale. This shift can be corrected using measured images of local muons, for which the light yield is predictable. Based on the prediction and the simulated light yield, an average energy correction factor is determined for the data of each of the three years separately. The resulting average values are 1.12 for 2003 and 2004, and 1.30 for 2005. These correction factors are used to correct the reconstructed energies thereby enabling direct comparisons between different years. Note that a correction factor is needed already for the first data set of 2003 since the Monte-Carlo simulations refer to new mirrors, but in 2003 the first HESS telescope was already one year old. In 2004, the total optical efficiency of the system remained the same because of the inclusion of two telescopes with nominal efficiency, thereby cancelling the aging effects of the first two telescopes.

The spectra shown in Fig. 3 are after correction. Very good agreement is found between the different years. The measured spectral shape remains unchanged over time. The absolute flux levels are well within the systematic uncertainty of 20%. As expected for an object like RX J1713.7–3946, no flux variation is seen on yearly timescales. Clearly, the performance of the telescope system is under good control, the correction of the optical degradation by means of energy correction factors determined from “muon efficiencies” works reasonably well (see also Aharonian et al. 2006c). Note that without correction of aging effects, flux differences between 2004 and 2005 are on the order 40%.

The combined data of three years are shown in Fig. 4. This energy spectrum of the whole SNR region corresponds to 91 h of HESS observations (*Data set III*, Table 1). It is generated analysing the 2003 data separately, with the *ON/OFF* approach and the two-telescope analysis. The 2004 and 2005 data are analysed together, with the *reflected-region* background and the nominal 80-photo-electrons cut. As shown in Table 1, a fraction of the data was recorded with wobble offsets smaller than 0.7° .

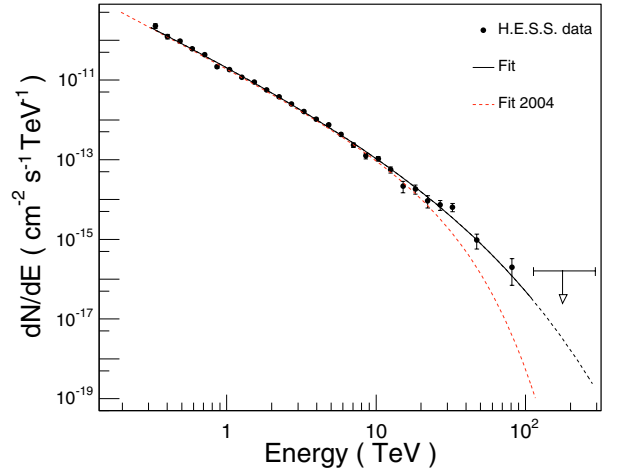


Fig. 4. Combined HESS gamma-ray spectrum of RX J1713.7–3946 generated from data of 2003, 2004, and 2005 (*Data set III*, Table 1). Data are corrected for the variation of optical efficiency. Error bars are $\pm 1\sigma$ statistical errors. These data might be described by a power law with exponential cutoff of the form $dN/dE = I_0 E^{-\Gamma} \exp(-E/E_c)^\beta$. The best fit result (black solid line) is given here for $\beta = 0.5$ (fixed), $\Gamma = 1.8$, and $E_c = 3.7$ TeV (cf. Table 4 for the exact values). Note that the fit function extends as dashed black line beyond the fit range for illustration. For comparison, the best fit of a power law with exponential cutoff and $\beta = 1$, obtained solely from the 2004 data (Aharonian et al. 2006b), is shown as dashed red line. A model-independent upper limit, indicated by the black arrow, is determined in the energy range from 113 to 294 TeV.

For this part, the *ON/OFF* method is applied. Average energy-correction factors for each of the three subsets of data separately are determined as explained above. Having analysed the data separately to obtain suitable background estimates for the SNR region, spectra are then combined to yield the final spectrum shown in Fig. 4. Systematic checks included the application of tighter cuts on the image amplitude to the 2004 and 2005 data and separate analysis of data recorded under small and large zenith angles (below and above 50°). While the spectra determined with different cuts are fully compatible, a slight flux overestimation is found for the large zenith-angle data, on the 10% level. The investigations of systematic uncertainties at the largest zenith angles are still underway, but since the effect on the final spectrum is small, $<5\%$, the combined spectrum given here includes all data, up to zenith angles of 70° .

The energy binning of the differential flux shown in the figure is chosen to be 12 bins per decade. For the final two points of the spectrum, beyond energies of 30 TeV, the binning is three times coarser, 4 bins per decade, accounting for decreasing event statistics at the highest energies. For the actual positioning of the flux points within an energy bin, the method proposed in Lafferty & Wyatt (1995) is adopted: the point appears at the

Table 4. Fit results for different spectral models. The fit range is chosen from 0.3 to 113 TeV. The differential flux normalisation I_0 is given in units of $10^{-12} \text{ cm}^{-2} \text{ s}^{-1} \text{ TeV}^{-1}$. Shown are a power-law model (row 1), a power law with an exponential cutoff (row 2, 3, 4; the cutoff energy E_c is given in TeV), a power law with an energy dependent photon index (row 5), and a broken power law (row 6; in the formula, the parameter $S = 0.6$ describes the sharpness of the transition from Γ_1 to Γ_2 and it is fixed in the fit). Note that when fitting a broken power law to the data, some of the fit parameters are highly correlated.

Fit Formula	Fit Parameters				χ^2 (d.o.f.)
$I_0 E^{-\Gamma}$	$I_0 = 20.5 \pm 0.4$	$\Gamma = 2.32 \pm 0.01$			145.6 (25)
$I_0 E^{-\Gamma} \exp\left(-\frac{E}{E_c}\right)^\beta$	$I_0 = 21.3 \pm 0.5$	$\Gamma = 2.04 \pm 0.04$	$E_c = 17.9 \pm 3.3$	$\beta = 1.0$	39.5 (24)
	$I_0 = 34.1 \pm 2.5$	$\Gamma = 1.79 \pm 0.06$	$E_c = 3.7 \pm 1.0$	$\beta = 0.5$	34.3 (24)
	$I_0 = 40.5 \pm 1.5$	$\Gamma = 1.74 \pm 0.02$	$E_c = 2.3 \pm 0.2$	$\beta = 0.45$	34.2 (24)
$I_0 E^{-\Gamma+\beta \log E}$	$I_0 = 20.6 \pm 0.5$	$\Gamma = 2.02 \pm 0.04$	$\beta = -0.29 \pm 0.03$	38.8 (24)	
$I_0 \left(\frac{E}{E_B}\right)^{-\Gamma_1} \left(1 + \left(\frac{E}{E_B}\right)^{1/S}\right)^{S(\Gamma_1-\Gamma_2)}$	$I_0 = 0.5 \pm 0.4$	$\Gamma_1 = 2.00 \pm 0.05$	$\Gamma_2 = 3.1 \pm 0.2$	$E_B = 6.6 \pm 2.2$	29.8 (23)

energy value, where the flux value predicted by an effective-area weighted model spectral shape (a power law with exponential cutoff) is equal to the mean flux value over the energy bin. Note that this is only relevant for wide bins. Here, for the spectrum of Fig. 4, the procedure results in flux points that are placed within 1% of the central energy value of the bin. Only for the two last points the difference is considerable, they end up at 7 and 12% smaller energy values than the bin centre.

The combined HESS spectrum of RX J1713.7–3946 shown in Fig. 4 extends over almost three decades in energy, and is compatible with previous HESS measurements. Kelner et al. (2006) have recently presented a new analytical expression (a modified exponential cutoff with exponent β) for secondary gamma-ray spectra from inelastic proton-proton interactions based on Monte-Carlo simulations. Table 4 provides the results of fitting this function, in addition to several other functional forms, to the data. A pure power-law model is clearly ruled out, the alternative spectral models provide significantly better descriptions of the data. For the modified exponential-cutoff shape, the exponent β was fixed at 1.0, 0.5 and 0.45. The latter β value was chosen because it yields the smallest χ^2 value. The cutoff energy of the gamma-ray spectrum was found to vary depending on β , values of ~ 18 TeV, ~ 3.7 TeV, and ~ 2.3 TeV were fit, and none of the three β values is statistically favoured over the other taking the value of χ^2 as measure. Under the assumption that indeed the VHE gamma rays are due to cosmic-ray protons interacting with ambient matter and subsequent π^0 decay, one might get an idea of the parameters of the parent proton spectrum. Following the approach of Kelner et al. (2006), proton cutoff values in the range of 50 to 150 TeV with spectral indices α ranging from 1.7 to 2.1 would be fully compatible with the gamma-ray data presented here. Note, however, that a proton cutoff in the 100 TeV range does not mean the spectrum terminates at this energy. Especially in case of a hard power-law index $\alpha < 2$ there would be a sufficient number of protons beyond the cutoff energy.

Combining the data of three years it is possible to extend the gamma-ray spectrum up to energies beyond 30 TeV. Taking all events with energies above 30 TeV, the cumulative significance is 4.8σ . Table 5 lists all the flux points together with bin-by-bin event statistics.

6. Summary and discussion

The complete HESS data set of the SNR RX J1713.7–3946 recorded from 2003 to 2005 is presented here. When analysing the data of different years separately and comparing them to each

other, a very good agreement is found for both the gamma-ray morphology and the differential energy spectra. The HESS telescope system obviously operates stably over the course of three years, if one takes known aging effects into account.

A combined gamma-ray image using ~ 63 h of HESS observations in 2004 and 2005 was generated achieving an unprecedented angular resolution of 0.06° . The morphology of RX J1713.7–3946 in VHE gamma rays confirms its earlier characterisation (Aharonian et al. 2006b) of a thick, almost circular shell structure with the brightest regions in the northwest, very similar to the X-ray image of this source. The gamma-ray spectrum of the combined HESS data over three years on RX J1713.7–3946 extends over three orders of magnitude in energy. Although at the edge of sufficient statistical significance, the high-energy end of the gamma-ray spectrum approaches 100 TeV with significant emission (4.8σ) beyond 30 TeV. Given the systematic uncertainties in the spectral determination at these highest energies and comparable statistical uncertainties despite the long exposure time, this measurement is presumably close to what can be studied with the current generation of imaging atmospheric Cherenkov telescopes.

From the largest measured gamma-ray energies one can estimate the corresponding energy of the primary particles. If VHE gamma rays are produced via π^0 decay following inelastic proton-proton interactions, gamma-ray energies of 30 TeV imply that primary protons are accelerated to $30 \text{ TeV}/0.15 = 200 \text{ TeV}$ in the shell of RX J1713.7–3946. On the other hand, if the gamma rays are due to Inverse Compton scattering of VHE electrons, accelerated in the shell, off Cosmic-Microwave-Background photons (neglecting the presumably small contributions from starlight and infrared photons), the electron energies at the current epoch can be estimated in the Thompson regime as $E_e \approx 20 \sqrt{E_\gamma} \text{ TeV} \approx 110 \text{ TeV}$. At these large energies Klein-Nishina effects start to be important and reduce the maximum energy slightly such that $\sim 100 \text{ TeV}$ is a realistic estimate.

If one considers the functional representations found for the fit of the gamma-ray spectrum of RX J1713.7–3946 (c.f. Table 4), the basic findings of Aharonian et al. (2006b) are confirmed with improved statistics and increased energy coverage: a pure power-law spectral shape is clearly ruled out, alternative models like a broken power-law, a power with energy-dependent exponent, and a power law with exponential cutoff describe the data significantly better. Assuming an exponential-cutoff shape, a “slow” cutoff with exponent $\beta = 0.5$, as suggested by detailed Monte-Carlo simulations (Kelner et al. 2006), yields a perfect description of the data, however,

Table 5. Flux points including relevant event statistics are listed for the spectrum of the combined HESS data set, shown in Fig. 4. For all 28 bins, the energy, the number of signal and background counts (ON and OFF), the normalisation factor α , the statistical significance σ , the gamma-ray flux and the energy range of the bin are given. The significance is calculated following Li & Ma (1983). For the final bin, as it has only marginally positive significance, we list both the actual flux point and the 2σ upper limit (which is drawn in Fig. 4). Note that the energy and flux values given here are corrected for the variation of optical efficiency, as discussed in the main text.

#	E (TeV)	ON	OFF	α	σ	Flux ($\text{cm}^{-2} \text{s}^{-1}$)	Range (TeV)
1	0.33	5890	5134	1.00	7.2	$(2.73 \pm 0.38) \times 10^{-10}$	0.30–0.37
2	0.40	5583	4797	1.00	7.7	$(1.48 \pm 0.19) \times 10^{-10}$	0.37–0.44
3	0.49	4878	4010	0.97	10.5	$(1.13 \pm 0.11) \times 10^{-10}$	0.44–0.54
4	0.59	4202	3409	0.94	11.6	$(7.22 \pm 0.63) \times 10^{-11}$	0.54–0.65
5	0.71	3900	2941	0.94	14.2	$(5.20 \pm 0.37) \times 10^{-11}$	0.65–0.79
6	0.86	3682	2833	0.97	11.9	$(2.56 \pm 0.22) \times 10^{-11}$	0.79–0.95
7	1.04	3881	2643	0.98	16.1	$(2.17 \pm 0.14) \times 10^{-11}$	0.95–1.15
8	1.26	3982	2758	0.97	16.0	$(1.40 \pm 0.09) \times 10^{-11}$	1.15–1.39
9	1.53	4076	2661	0.98	17.9	$(1.06 \pm 0.06) \times 10^{-11}$	1.39–1.69
10	1.85	3873	2603	0.97	17.0	$(6.71 \pm 0.40) \times 10^{-12}$	1.69–2.04
11	2.24	3452	2251	0.98	16.8	$(4.50 \pm 0.27) \times 10^{-12}$	2.04–2.47
12	2.71	3215	2113	0.98	15.9	$(2.97 \pm 0.19) \times 10^{-12}$	2.47–2.99
13	3.28	3075	2081	0.98	14.6	$(1.95 \pm 0.13) \times 10^{-12}$	2.99–3.63
14	3.98	2915	2057	0.98	12.9	$(1.24 \pm 0.10) \times 10^{-12}$	3.63–4.39
15	4.81	2537	1721	0.98	13.1	$(8.91 \pm 0.68) \times 10^{-13}$	4.39–5.31
16	5.82	2183	1555	0.98	10.8	$(5.18 \pm 0.48) \times 10^{-13}$	5.31–6.43
17	7.05	1961	1525	0.98	7.9	$(2.77 \pm 0.35) \times 10^{-13}$	6.43–7.79
18	8.53	1507	1208	0.98	6.2	$(1.49 \pm 0.24) \times 10^{-13}$	7.79–9.43
19	10.33	1211	881	0.98	7.6	$(1.27 \pm 0.17) \times 10^{-13}$	9.43–11.41
20	12.51	881	664	0.99	5.8	$(6.69 \pm 1.15) \times 10^{-14}$	11.41–13.81
21	15.14	652	551	0.99	3.2	$(2.58 \pm 0.82) \times 10^{-14}$	13.81–16.72
22	18.32	473	364	0.99	4.0	$(2.19 \pm 0.55) \times 10^{-14}$	16.72–20.24
23	22.18	327	260	0.99	2.9	$(1.10 \pm 0.38) \times 10^{-14}$	20.24–24.50
24	26.85	220	153	0.99	3.6	$(8.82 \pm 2.46) \times 10^{-15}$	24.50–29.66
25	32.50	182	110	0.99	4.3	$(7.70 \pm 1.79) \times 10^{-15}$	29.66–35.91
26	47.19	227	180	0.99	2.5	$(1.15 \pm 0.47) \times 10^{-15}$	35.91–63.71
27	81.26	51	37	0.99	1.5	$(2.36 \pm 1.55) \times 10^{-16}$	63.71–113.02
28	169.79	14	11	1.00	0.6	$(3.77^{+6.39}_{-3.77}) \times 10^{-17}$	113.02 – 293.82
					Upper Limit	1.6×10^{-16}	

different values of β cannot be distinguished, but would rather require better event statistics at the highest energies.

Given the good agreement of the results presented here with the previously published ones, our restrictive conclusions regarding the nature of the parent particles remain unchanged to those outlined in Aharonian et al. (2006b). Both scenarios with a leptonic, or hadronic primary particle distribution are able to accommodate an exponential-cutoff shape with an index of $\beta \sim 0.5$. However, if the mean magnetic field in the SNR region is indeed strongly amplified by the shock to values well beyond typical interstellar fields, the hadronic nature of the observed gamma-ray emission would be difficult to conceal and this latter emission scenario would be clearly favoured (Berezhko & Völk 2006).

With the deep HESS observations of RX J1713.7–3946 we approach now energies, at which attenuation due to pair production on the Galactic interstellar radiation field begins to affect the gamma-ray spectrum (Zhang et al. 2006). At the currently measured maximum energy this effect is negligible, particularly since RX J1713.7–3946 is neither in the direction of the Galactic center (more than 12° angular separation in line-of-sight), nor is it at the distance where the interstellar radiation field peaks (Moskalenko et al. 2006). RX J1713.7–3946 will therefore presumably not be the astronomical source, where we will obtain a clear observational confirmation of the attenuation of gamma rays due to the interstellar radiation field. However, RX J1713.7–3946 remains an exceptional SNR in respect of

its VHE gamma-ray observability, being at present the remnant with the widest possible coverage along the electromagnetic spectrum. The HESS measurement of significant gamma-ray emission beyond 30 TeV without indication of a termination of the high-energy spectrum provides proof of particle acceleration in the shell of RX J1713.7–3946 beyond 10^{14} eV, up to energies which start to approach the region of the cosmic-ray *knee*.

Acknowledgements. The support of the Namibian authorities and of the University of Namibia in facilitating the construction and operation of HESS is gratefully acknowledged, as is the support by the German Ministry for Education and Research (BMBF), the Max Planck Society, the French Ministry for Research, the CNRS-IN2P3 and the Astroparticle Interdisciplinary Programme of the CNRS, the UK Particle Physics and Astronomy Research Council (PPARC), the IPNP of the Charles University, the South African Department of Science and Technology and National Research Foundation, and by the University of Namibia. We appreciate the excellent work of the technical support staff in Berlin, Durham, Hamburg, Heidelberg, Palaiseau, Paris, Saclay, and in Namibia in the construction and operation of the equipment.

References

- Aharonian, F., Akhperjanian, A. G., Aye, K. M., et al. (HESS Collaboration) 2004a, *A&A*, 22, 109
- Aharonian, F., Akhperjanian, A. G., Aye, K. M., et al. (HESS Collaboration) 2004b, *Nature*, 432, 75
- Aharonian, F., Akhperjanian, A. G., Bazer-Bachi, A. R., et al. (HESS Collaboration) 2005a, *A&A*, 437, L7
- Aharonian, F., Akhperjanian, A. G., Aye, K. M., et al. (HESS Collaboration) 2005b, *A&A*, 430, 865

- Aharonian, F., et al. (HESS Collaboration) 2006a, *ApJ*, submitted
- Aharonian, Akhperjanian, A. G., Bazer-Bachi, A. R., et al. (HESS Collaboration) 2006b, *A&A*, 449, 223
- Aharonian, F., Akhperjanian, A. G., Bazer-Bachi, A. R., et al. (HESS Collaboration) 2006c, *A&A*, 457, 899
- Berezhko, E. G., & Völk, H. J. 2006, *A&A*, 451, 981
- Berge, D. 2006, Ph.D. Thesis, Ruprecht-Karls Universität, Heidelberg, <http://www.ub.uni-heidelberg.de/archiv/6156>
- Bernlöhr, K., Carrol, O., Cornils, R., et al. 2003, *Astropart. Phys.*, 20, 111
- Cornils, R., Gillessen, S., Jung, I., et al. 2003, *Aph*, 20, 129
- Drury, L. O., Aharonian, F. A., & Voelk, H. J. 1994, *A&A*, 287, 959
- Funk, S., Hermann, G., Hinton, J., et al. 2004, *Astropart. Phys.*, 22, 285
- Hillas, A. M. 2005, *J. Phys. G Nucl. Phys.*, 31, R95
- Hinton, J., Berge, D., & Funk, S. 2005, in *Conference Proceedings Towards a Network of Atmospheric Cherenkov Detectors VII*, Palaiseau, France
- Hiraga, J. S., Uchiyama, Y., Takahashi, T., & Aharonian, F. A. 2005, *A&A*, 431, 953
- Hofmann, W., Jung, I., Konopelko, A., et al. 1999, *Astropart. Phys.*, 12, 135
- Hofmann, W. (HESS Collaboration) 2005, in *Conference Proceedings Towards a Network of Atmospheric Cherenkov Detectors VII*, Palaiseau, France, 43
- Kelner, S. R., Aharonian, F. A., & Bugayov, V. V. 2006, *Phys. Rev. D*, 74, 034018
- Lafferty, G. D., & Wyatt, T. R. 1995, *Nucl. Instrum. Methods Phys. Res. A*, 355, 541
- Li, T.-P., & Ma, Y.-Q. 1983, *ApJ*, 272, 317
- Moskalenko, I. V., Porter, T. A., & Strong, A. W. 2006, *ApJ*, 640, L155
- Uchiyama, Y., Takahashi, T., & Aharonian, F. A. 2002, *PASJ*, 54, L73
- Vincent, P., et al. (HESS Collaboration) 2003, in *Proc. 28th ICRC*, 2887
- Zhang, J.-L., Bi, X.-J., & Hu, H.-B. 2006, *A&A*, 449, 641
- ⁷ DAPNIA/DSM/CEA, CE Saclay, 91191 Gif-sur-Yvette, Cedex, France
- ⁸ University of Durham, Department of Physics, South Road, Durham DH1 3LE, UK
- ⁹ Unit for Space Physics, North-West University, Potchefstroom 2520, South Africa
- ¹⁰ Laboratoire Leprince-Ringuet, IN2P3/CNRS, Ecole Polytechnique, 91128 Palaiseau, France
- ¹¹ Laboratoire d'Annecy-le-Vieux de Physique des Particules, IN2P3/CNRS, 9 Chemin de Bellevue, BP 110, 74941 Annecy-le-Vieux Cedex, France
- ¹² APC, 11 Place Marcelin Berthelot, 75231 Paris Cedex 05, France/UMR 7164 (CNRS, Université Paris VII, CEA, Observatoire de Paris).
- ¹³ Dublin Institute for Advanced Studies, 5 Merrion Square, Dublin 2, Ireland
- ¹⁴ Landessternwarte, Universität Heidelberg, Königstuhl, 69117 Heidelberg, Germany
- ¹⁵ Laboratoire de Physique Théorique et Astroparticules, IN2P3/CNRS, Université Montpellier II, CC 70, Place Eugène Bataillon, 34095 Montpellier Cedex 5, France
- ¹⁶ Universität Erlangen-Nürnberg, Physikalisches Institut, Erwin-Rommel-Str. 1, 91058 Erlangen, Germany
- ¹⁷ Laboratoire d'Astrophysique de Grenoble, INSU/CNRS, Université Joseph Fourier, BP 53, 38041 Grenoble Cedex 9, France
- ¹⁸ Institut für Astronomie und Astrophysik, Universität Tübingen, Sand 1, 72076 Tübingen, Germany
- ¹⁹ Laboratoire de Physique Nucléaire et de Hautes Energies, IN2P3/CNRS, Universités Paris VI & VII, 4 Place Jussieu, 75252 Paris Cedex 5, France
- ²⁰ Institute of Particle and Nuclear Physics, Charles University, V Holesovickach 2, 180 00 Prague 8, Czech Republic
- ²¹ Institut für Theoretische Physik, Lehrstuhl IV: Weltraum und Astrophysik, Ruhr-Universität Bochum, 44780 Bochum, Germany
- ²² University of Namibia, Private Bag 13301, Windhoek, Namibia
- ²³ European Associated Laboratory for Gamma-Ray Astronomy, jointly supported by CNRS and MPG
-
- ¹ Max-Planck-Institut für Kernphysik, PO Box 103980, 69029 Heidelberg, Germany
e-mail: David.Berge@cern.ch
- ² Yerevan Physics Institute, 2 Alikhanian Brothers St., 375036 Yerevan, Armenia
- ³ Centre d'Etude Spatiale des Rayonnements, CNRS/UPS, 9 av. du Colonel Roche, BP 4346, 31029 Toulouse Cedex 4, France
- ⁴ Universität Hamburg, Institut für Experimentalphysik, Luruper Chaussee 149, 22761 Hamburg, Germany
- ⁵ Institut für Physik, Humboldt-Universität zu Berlin, Newtonstr. 15, 12489 Berlin, Germany
- ⁶ LUTH, UMR 8102 du CNRS, Observatoire de Paris, Section de Meudon, 92195 Meudon Cedex, France